RSC Advances

PAPER

View Article Online
View Journal | View Issue

Cite this: *RSC Adv.*, 2026, **16**, 23430

Valorization of silicon cutting waste and high-alumina fly ash for sustainable synthesis of O′-sialon

Hao Wang, *[a] Xinlin Zhai,[a] Lili Liu,[b] Yin Jiang[c] and Yi Xing[a]

This study presents a sustainable route for preparing O′-Sialon ceramics from silicon cutting waste (SCW) and high-alumina fly ash (HAFA). SCW was used as the main reactive Si-bearing waste, whereas HAFA provided Al-containing and Si-containing mineral phases. The effects of sintering temperature (1250–1450 °C) and holding time (1–9 h) on phase evolution, microstructure, and macroscopic properties were systematically investigated. XRD results indicate that an O′-Sialon-dominant product was obtained at 1350 °C, while higher temperatures promoted the formation of β-Sialon. The sample sintered at 1350 °C for 5 h showed a bulk density of 1.95 g cm^{-3}, a linear shrinkage of 11.75%, a compressive strength of 88.55 MPa, and a porosity of 30.32%. Thermodynamic analysis together with phase and microstructural characterization further suggests that Ca was mainly incorporated into Ca-containing SiAlON-related phases, whereas Fe was mainly stabilized as Fe_3Si under the present processing conditions. These results demonstrate the feasibility of up-cycling SCW and HAFA into value-added SiAlON-based ceramics, while also highlighting the need for future work on raw-material variability and scale-up.

Received 18th December 2025
Accepted 24th April 2026

DOI: 10.1039/d5ra09795a

rsc.li/rsc-advances

1. Introduction

Silicon cutting waste (SCW) is a by-product generated during the process of silicon cutting, containing abundant silicon carbide particles and silicon particles. With the rapid growth of the solar photovoltaic industry, there has been a gradual increase in SCW production. However, the lack of effective recycling methods for its disposal leads to significant environmental pollution and resource wastage problems.[1–3] Currently, a significant number of researchers are engaged in conducting extensive investigations on the recovery methods of SCW.[4] At this stage, the recycling approaches for SCW can be categorized into two distinct groups: high value-added Si separation and direct synthesis of high value-added materials. Wei *et al.*[5] used a simple and efficient method to extract Si from silicon cutting waste at a lower temperature (1000–1200 °C), while using cryolite to enhance the extraction of Si. Wang *et al.*[6] used centrifugal enhanced phase separation means to efficiently separate SiC and Si from SCW, and the phase separation time could be shortened from 460 min to 2 min in a normal gravity field at a supergravity factor *G* of 100, and the effects of emulsified oil droplet diameter and centrifugal force on phase separation were investigated with theoretical calculations. Li *et al.*[7] used a combination of electromagnetic and slag treatment ($CaO–SiO_2–Na_3AlF_6$) techniques to separate and purify Si from crystalline silicon cutting waste, and the purity of separated Si was improved from 88.01% to 99.47% compared with conventional high-temperature treatment, and the purity of separated Si could reach 99.98% after further vacuum directed solidification treatment.

Although the separation of silicon products from SCW offers significant added value, there are certain challenges in the recovery process that restrict the widespread application of these methods, such as substantial raw material requirements, high separation costs, and product impurities.[8,9] In contrast, direct resource utilization of SCW eliminates intricate separation steps, reduces production costs, and enables the preparation of highly valuable products like silicon carbide, silicon nitride ceramics, and silicon nitride composites.[10,11] Hou *et al.*[12] employed the direct nitriding method using diamond wire cutting polysilicon waste to synthesize α-Si_3N_4, and investigated the influence of $FeCl_3$, NaCl, and Cu metal on the nitridation process. Interestingly, Cu metal was identified as the most effective catalyst for promoting the nitriding reaction. Jin *et al.*[13] through thermodynamic calculations and density functional theory analysis, elucidated the acceleration mechanism of sintering temperature and CaO addition on the nitridation reaction. Furthermore, they successfully fabricated Si_3N_4 ceramics with remarkable properties including a bulk density of 2.31 g cm^{-3}, an apparent porosity of 25.42%, and a compressive strength of 109 MPa when incorporating 5 wt% CaO additives. Sun *et al.*[14] employed the atmospheric pressure electromagnetic induction heating method to synthesize SiC/α-Si_3N_4 composite powder. The addition of NH_4Cl was found to effectively promote

[a]*School of Energy and Environmental Engineering, University of Science & Technology Beijing, Beijing, 100083, PR China. E-mail: wanghao@ustb.edu.cn*

[b]*School of Materials Science and Engineering, Peking University, Beijing 100871, PR China*

[c]*China Academy of Safety Science and Technology, Beijing100012, PR China*

the nitridation reaction by precisely controlling the reaction temperature and actively participating in the reaction process. Furthermore, it was observed that the presence of Fe_2O_3 impurities significantly facilitated the formation of α-Si_3N_4 during the reaction.

The Sialon material, primarily composed of Si_3N_4–Al_2O_3–AlN–SiO_2, has garnered significant attention in the field of refractory materials due to its exceptional performance. It encompasses four categories: O′-Sialon, α-Sialon, β-Sialon, and X-Sialon.[15] Among these categories, O′-Sialon ($Si_{2-x}Al_xO_{1+x}N_{2-x}$, $0 < x < 0.4$) has received considerable interest owing to its outstanding oxidation resistance, thermal shock resistance, and slag corrosion resistance. Numerous scholars have conducted relevant research on this material.[16] For instance, Ma *et al.*[17] sintered Si_3N_4/O′-Sialon ceramics with varying SiO_2 contents under a pressure of 3 MPa. An *et al.*[18] on the other hand, prepared mullite-SiC-O′-Sialon composites using bauxite-based homogeneous mullite as well as silica powder and phenolic resin as raw materials.

In this study, SCW and HAFA were coupled to explore a direct and waste-oriented route for preparing O′-Sialon ceramics. Compared with conventional recovery-first strategies, the present approach avoids prior separation of Si from SCW and instead uses SCW as the major reactive silicon source, while HAFA supplies Al-rich and Si-rich mineral phases. The study focuses on the influence of sintering temperature and holding time on phase evolution, microstructure, and properties, together with the migration behavior of the main impurity elements. It should be emphasized that this work is a laboratory-scale feasibility study rather than an immediate industrial implementation route. Because fly ash is inherently heterogeneous and contains minor impurities, additional work will be required on feedstock variability, pretreatment, process scale-up, and secondary-waste minimization before practical application. Nevertheless, the present results provide a useful basis for the valorization of SCW and HAFA into low-cost SiAlON-based ceramic materials.

2. Materials and methods

2.1 Materials

The raw materials used in this work were silicon cutting waste (SCW) and high-alumina fly ash (HAFA). SCW was obtained from a silicon wafer manufacturer in Lianyungang, China, and HAFA was collected from the ash-storage system of a coal-fired power plant in Shuozhou, China. Both wastes were dried at 110 °C for 12 h and ground to pass 200 mesh before use. The chemical composition of the raw materials was analyzed by XRF, and their crystalline phases were identified by XRD. The detailed characterization results are presented in Section 3.1.

2.2 Methods

The chemical formula of O′-Sialon is $Si_{2-x}Al_xO_{1+x}N_{2-x}$, where x ranges from 0 to 0.4. Considering the composition characteristics of solid waste SCW and HAFA in this study, as well as the material balance calculation results of high-temperature carbon thermal reduction nitridation reaction, a waste component compatibility scheme with a ratio of 50 : 50 is designed. Additionally, 3% graphitic carbon is incorporated as a carbon source for the carbon thermal reduction nitridation reaction to ensure the attainment of O′-Sialon composition under high-temperature reaction conditions from a material balance perspective. The experimental procedure commenced by subjecting the prepared raw materials to planetary ball milling for 10 hours as per the designed composition formula. Subsequently, the thoroughly mixed powder was compacted into cylindrical molds (Φ 40 mm, H 5 mm) under a pressure of 5 MPa before being subjected to high-temperature heat treatment in a furnace. The heat treatment process parameters are presented in Table 1. The entire heat treatment procedure involves maintaining a nitrogen gas flow rate of 0.5 L min^{-1} within the temperature range of 1250–1450 °C, with an holding time ranging from 1 to 9 hours at the target temperature. The heating rate during the process is set at 10 °C min^{-1}, followed by furnace cooling and subsequent removal of the samples after completion of the holding period.

Table 1 Heat treatment experimental design proposal for samples

Sample ID	Heat treatment temperature (°C)	Holding time (h)
1	1250	5
2	1300	5
3	1350	5
4	1400	5
5	1450	5
6	1350	1
7	1350	3
8	1350	7
9	1350	9

2.3 Characterization

The thermal behavior of raw materials at high sintering temperature was investigated using thermogravimetric-differential scanning calorimetry (TG-DSC, S60, SETARAM, France). The TG-DSC

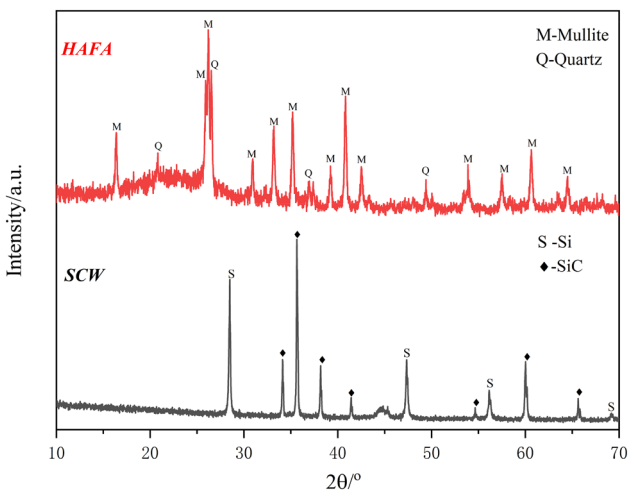

Fig. 1 The XRD result of raw materials.

measurements were carried out from 20 to 1300 °C at a heating rate of 5 °C min under an N_2 atmosphere. The chemical composition of the raw materials was analyzed by X-ray fluorescence (XRF, Axios mAX, PANalytical, Netherlands), while the crystal phase composition of both the raw materials and samples was determined through X-ray diffraction (XRD, D/max 2550, Rigaku, Japan) over a 2θ range of 10–70° at a scanning rate of 4° min^{-1}. For SEM observation, small fragments produced after the compressive-strength test were collected and etched with HF to reveal the grain morphology more clearly. The etched fragment surfaces were then sputter-coated with Au to enhance conductivity prior to imaging. SEM micrographs were collected on a Hitachi S-4800 instrument using secondary electron (SE) mode. Bulk density and porosity were measured by the oil-immersion method according to QB/T 1642–2012 using kerosene as the immersion medium. Three samples were tested for each condition and the average value was reported. Linear shrinkage was determined from the dimensional change before and after sintering. Compressive strength was measured using an electronic universal testing machine (UTM5105, Shenzhen, China), and the compressive strength (σ_b) was calculated from the maximum load at failure (F) and the loaded area of the specimen (S).

$$\sigma_b = F/S \quad (1)$$

3. Results and discussion

3.1 Raw material characterization of SCW and HAFA

During the process of cutting silicon wafers, silicon carbide is primarily utilized as an abrasive. Some SiC particles also enter into the polishing waste during the polishing process. Therefore, in SCW, there are not only single crystal silicon components but also some SiC components present. XRD analysis reveals that its phase composition structure mainly consists of Si (Si, #03-065-1060) and SiC (SiC, #01-089-2640). Combined with XRF analysis, it can be observed that each component's content is Si (38.126 wt%) and SiC (59.963 wt%), along with a small amount of Al_2O_3 (1.723 wt%). Additionally, in HAFA, XRF analysis results demonstrate that it primarily comprises of SiO_2 (47.998 wt%) and Al_2O_3 (38.373 wt%) components with a minor quantity of CaO (4.607 wt%) and Fe_2O_3 (3.399 wt%) components present. The XRD outcomes indicate that its primary crystal phases are mullite ($Al_6Si_2O_{13}$, #01-079-1454) and quartz (SiO_2, #01-075-0443).

3.2 Thermodynamic analysis of heat treatment processes

To ensure the synthesis of O′-Sialon, the high-temperature thermal properties of the mixed raw materials were analyzed first, and the result was shown in Fig. 2. Because the TG-DSC tests were conducted under N_2, the thermal-analysis atmosphere was consistent with the atmosphere used in the sintering experiments. In this result we can see that the TG-DSC results can be roughly divided into three temperature stages. In the first temperature stage (room temperature-1155 °C), it can be seen that the sample mass increased steadily, and this enormous mass increase reached 23.9 wt%. Based on the analysis of raw material composition characteristics in Table 1 and Fig. 1, the raw material for the monatomic silicon component exhibits high temperature reactivity, enabling reactions with graphitic carbon and N_2 atmosphere to produce silicon carbide and silicon nitride. Additionally, it can react with SiO_2 to form Si_2N_2O components. Thermodynamic equilibrium calculations confirm the feasibility of these reactions within this temperature range. The potential chemical reaction equations are presented below.[19–21]

$$Si + C \rightarrow SiC \quad (2)$$

$$3Si + 2N_2 \rightarrow Si_3N_4 \quad (3)$$

$$3Si + 2N_2 + SiO_2 \rightarrow 2Si_2N_2O \quad (4)$$

$$2SiO_2 + 3C + N_2 \rightarrow Si_2N_2O + 3CO \quad (5)$$

$$SiC + SiO_2 + N_2 \rightarrow Si_2N_2O + CO \quad (6)$$

In the second temperature stage (1155–1345 °C), a 2.68 wt% weight decrease can be seen in the mass curve, where the decrease in mass was mainly due to the decomposition of calcium sulfate in the fly ash as well as the reaction between some of the SiO_2 and graphitic carbon.[22,23]

$$2CaSO_4 \rightarrow 2CaO + 2SO_2 + O_2 \quad (7)$$

$$SiO_2 + 3C \rightarrow SiC + 2CO \quad (8)$$

$$2SiO_2 + 3C + N_2 \rightarrow Si_2N_2O + 3CO \quad (9)$$

In the final stage (1345–1480 °C), the mass curve exhibits fluctuating changes in mass, and two exothermic peaks of crystallization are observed at temperatures of 1356 °C and 1405 °C, respectively. After careful analysis, it is hypothesized that the synthesis reactions of O′-Sialon and β-Sialon occur during this temperature range.[24] Significantly, the mass decrease in this stage may be attributed to ongoing reactions taking place across both low-temperature and high-temperature sections throughout the heating process. Additionally, the mass loss observed in this stage may also be associated with phase transformation processes, such as the partial transformation of O′-Sialon to β-Sialon, taking place at elevated temperatures.[25] Assuming an x value of 0.20 for O′-Sialon and a z value of 0.6 for β-Sialon, the reaction process can be illustrated as follows. However, further validation through post-sintering experiments is necessary to confirm the accuracy of our analysis (Fig. 2).

$$0.9Si_2N_2O + 0.1Al_2O_3 \rightarrow Si_{1.8}Al_{0.2}O_{1.2}N_{1.8} \quad (10)$$

$$Si_{1.8}Al_{0.2}O_{1.2}N_{1.8} + N_2 \rightarrow Si_{5.4}Al_{0.6}O_{0.6}N_{7.4} + 1.5O_2 \quad (11)$$

3.3 The effect of heat treatment temperature

Based on the thermal analysis of the raw materials' sintering process, an experimental program was designed to investigate the influence of heat treatment temperature. The heat

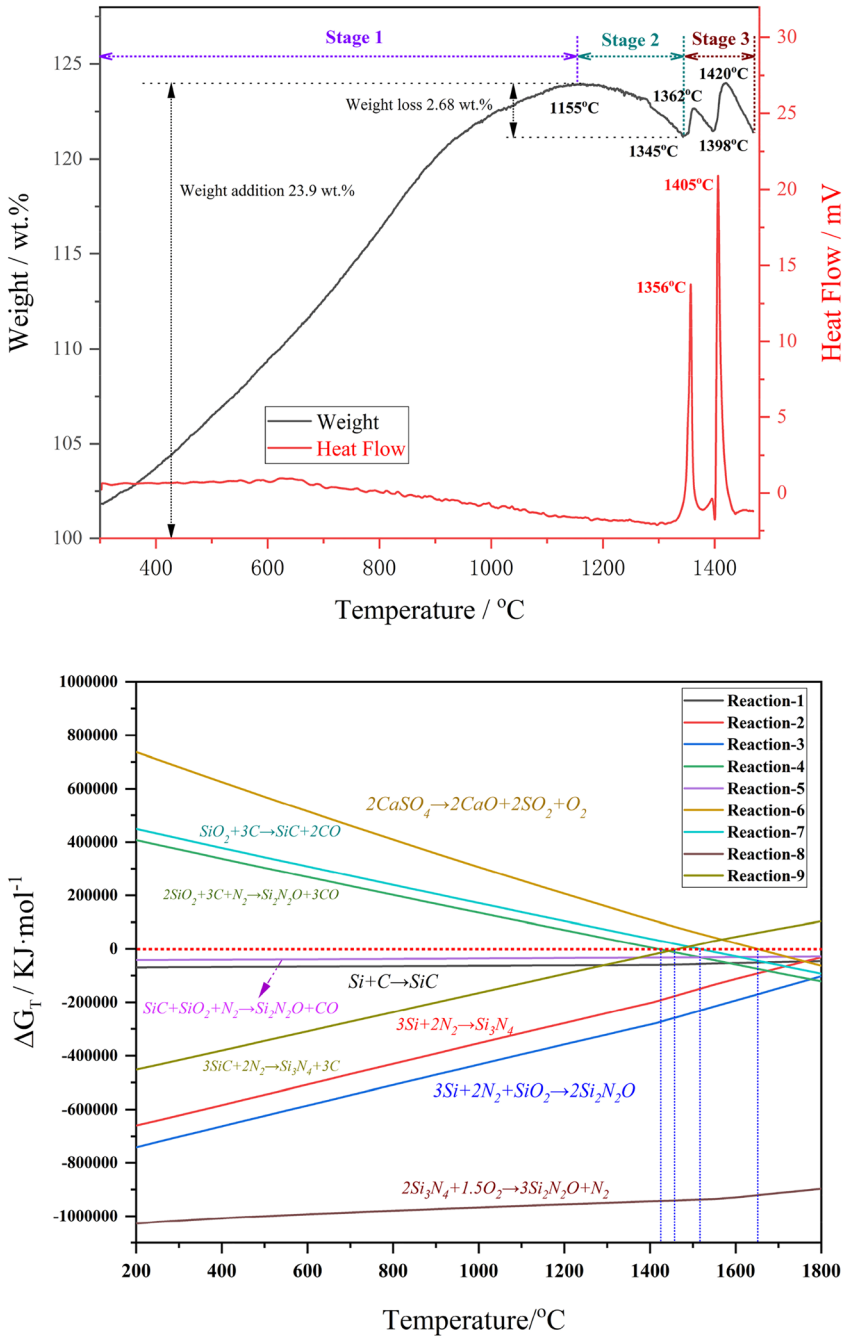

Fig. 2 The TG-DSC result of mixed raw materials and the Gibbs free energy of each reaction.

treatment temperature range was set between 1250–1450 °C. The impact of heat treatment temperature on the final physical phase structure was analyzed, and the results are presented in Fig. 3. It is evident from the figure that different heat treatment temperatures significantly affect the composition of the physical phase. Specifically, at a minimum treatment temperature of 1250 °C, the crystalline phase composition primarily consists of Si, Si_2N_2O, SiC, and mullite phases. Considering the composition analysis of raw material's physical phase, it can be observed that Si and mullite are inherent components in its physical phase. Upon heating to 1250 °C, graphitic carbon reacts with a portion of Si to form SiC phase while some quartz component generates Si_2N_2O from Si mono component. However, based on XRD peak spectrum intensity analysis, both synthesized SiC and Si_2N_2O contents were relatively low.

As the sintering temperature increased to 1300 °C, it is evident that the peak intensity of the monocrystalline silicon crystal phase decreased, while simultaneously, there was an increase in the peak intensity of the Si_2N_2O phase. This observation suggests that higher temperatures accelerate the synthesis of Si_2N_2O phase and demonstrate a favorable promotion effect on the reaction. Additionally, a few

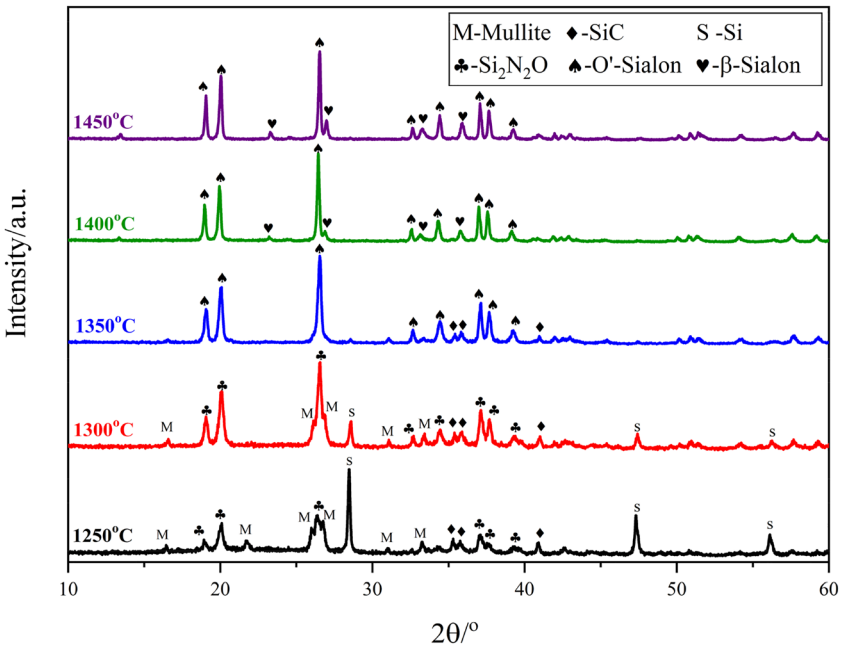

Fig. 3 The XRD results of samples sintered at various temperatures.

characteristic peaks corresponding to SiC phase and mullite phase were observed at this temperature, indicating that 1250 °C and 1300 °C are insufficient for synthesizing the desired products; thus, necessitating further elevation of sintering temperature.

When the samples were sintered at 1350 °C, a significant alteration in the physical phase composition was observed compared to the low-temperature sintering treatment. This observation indicates that the phase assemblage became dominated by O′-Sialon, accompanied by a minor SiC phase. Therefore, 1350 °C can be regarded as the key temperature for the formation of an O′-Sialon-dominant product in the present system. Furthermore, this finding aligns with the TG-DSC results aforementioned, which reveal an exothermic peak precipitation occurring precisely at 1356 °C and further substantiating the generation of O′-Sialon phase at this temperature.

With the further increase in sintering temperature, the formation of β-Sialon phase was observed at 1400 °C and 1450 °C. The content of β-Sialon phase gradually increased with higher sintering temperatures. According to semi-quantitative analysis, the content of β-Sialon phase increased from 12% to 30% between 1400 °C and 1450 °C. The appearance of β-Sialon phase at 1400 °C corresponds to the exothermic peak observed during crystallization at 1405 °C in the TG-DSC results. This observation confirms that O′-Sialon can transform into β-Sialon phase through a high-temperature reaction, as mentioned in the result of TG-DSC. Furthermore, it provides evidence for the mass fluctuation observed in TG results being attributed to Sialon's crystalline transition (Fig. 4).

The influence of different heat treatment temperatures on the properties of the materials in this study was further investigated, with a focus on shrinkage rate, porosity, bulk density, and compressive strength as key parameters examined. Overall, the results indicate that increasing sintering temperature promotes densification of the material. The shrinkage rate increased from 10.75% to 13.95%, accompanied by a decrease in porosity from 35.05% to 24.18%. Meanwhile, the bulk density increased from 1.82 g cm^{-3} to 2.12 g cm^{-3}, and the compressive strength increased from 72.10 MPa to 104.7 MPa. These performance indexes surpass those reported for Si_3N_4 materials mentioned previously in literature reviews. Combined with XRD phase analysis findings, it can be observed that as sintering temperature increases, there is a gradual transition in phase structure from Si monomers towards O′-Sialon phase and composite phases of O′-Sialon and β-Sialon compounds; this change positively impacts material performance improvement. Furthermore, composite phase materials exhibit greater strength compared to single physical phase counterparts.[26,27]

Representative SEM micrographs of HF-etched fragment surfaces of samples sintered at different temperatures are shown in Fig. 5. From a holistic perspective, an increase in sintering temperature exhibits a corresponding upward trend in overall sample density, which aligns with the aforementioned strength findings. Specifically, EDS analysis combined with XRD results reveals that at 1250 °C during low-temperature sintering (Fig. 5(a)), the microstructure is still dominated by monocrystalline silicon particles together with mullite-related phases inherited from the fly ash. As the treatment temperature rises, fine grains emerge within the microscopic morphology at 1300 °C; compositional analysis confirms their primary composition as Si_2N_2O. With a further increase in the treatment temperature to 1350 °C, the grain size exhibits growth and assumes a short columnar shape. EDS analysis reveals that the grains consist of O′-sialon crystal phase. At 1450 °C, the grain size transitions from short columnar to long columnar,

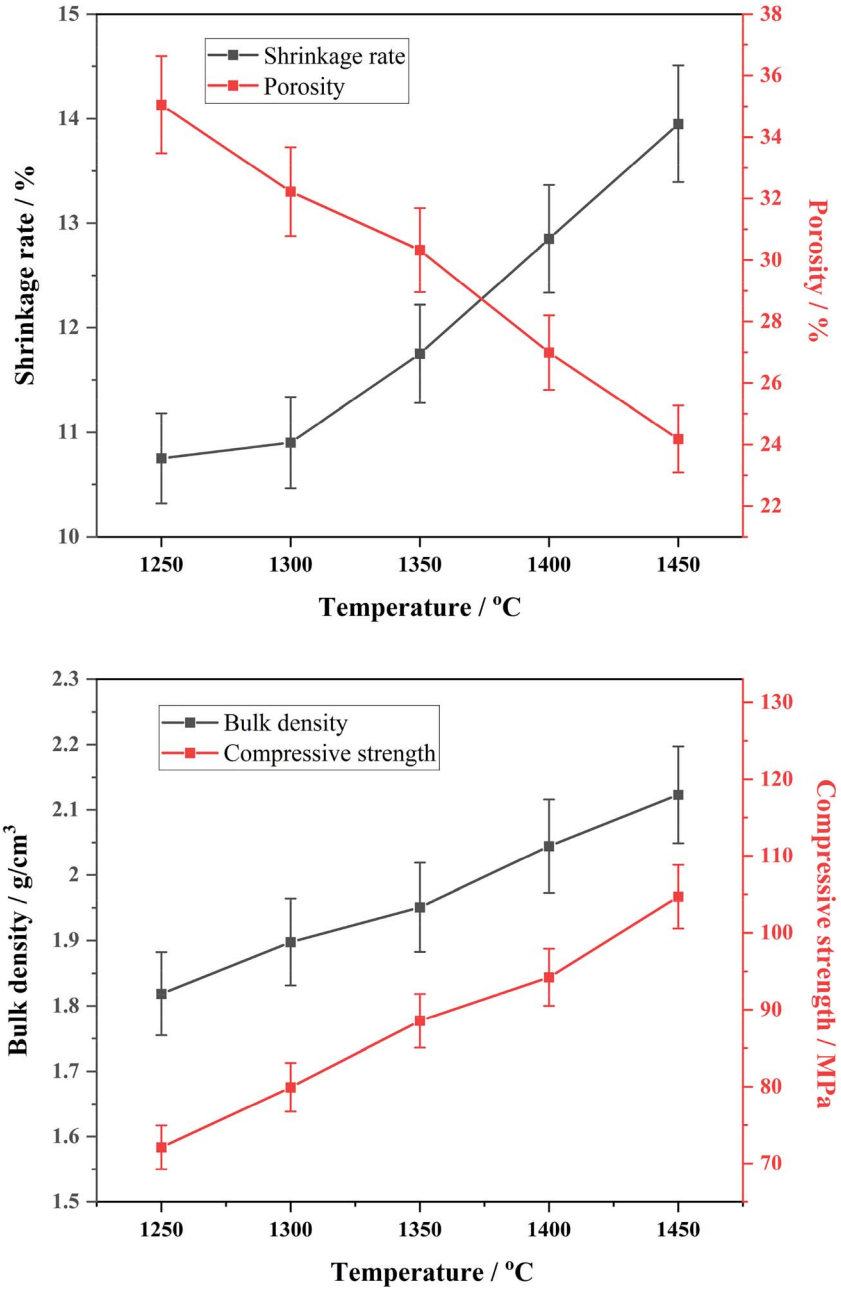

Fig. 4 The shrinkage rate, porosity, bulk density and compressive strength of samples sintered at various temperatures.

indicating that an elevated sintering temperature promotes grain enlargement as reported by Yan *et al.*[28] The toughening effect of sialon grains strengthens with an increasing length-to-diameter ratio, suggesting favorable toughness characteristics for this material. Simultaneously, a greater amount of glassy or liquid-phase-derived material can be observed around the grains and along the intergranular regions, indicating that impurities present in the raw materials underwent partial melting at this temperature. This phenomenon not only facilitates densification during sintering, but also enhances intergranular bonding through the formation of a glassy phase around the grains and along grain boundaries. The overall alterations in micro-morphology and corresponding changes in properties further demonstrate a substantial augmentation in material strength.[29,30]

3.4 The effect of holding time

After determining the temperature required for formation of the target phase assemblage, 1350 °C was selected to investigate the influence of holding time (1–9 h) on the phase evolution, microstructure, and properties of the material.

Firstly, in terms of the physical phase composition, Fig. 6 illustrates significant changes observed. Overall, it is evident that the material's physical phase composition undergoes

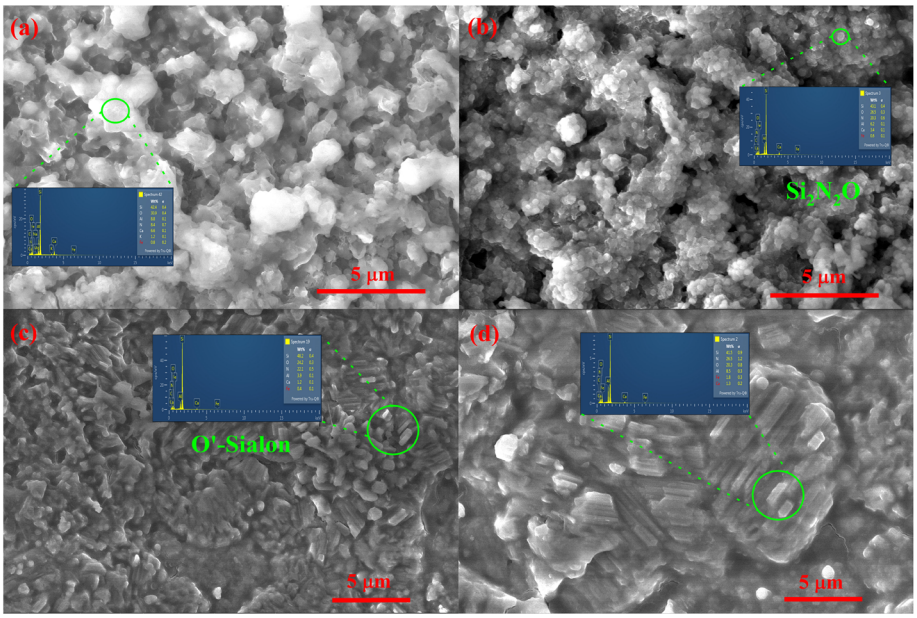

Fig. 5 SEM micrographs of HF-etched fragment surfaces of samples sintered at various temperatures: (a) 1250 °C, (b) 1300 °C, (c) 1350 °C, and (d) 1450 °C.

substantial alterations with varying holding times. A detailed analysis reveals that when subjected to a 1 hour holding time treatment, the predominant crystalline phases are mullite, Si, Si_2N_2O and SiC phases. At a holding time of 1 h, only part of the SCW and fly ash participates in the reaction, resulting in limited formation of Si_2N_2O and SiC, whereas the target O′-Sialon phase is still not detected. This indicates that the reaction is still in an intermediate stage at short holding times. With the increase in sintering holding time, it is evident from the results that the peak intensity of Si phase decreases while the peak intensity of Si_2N_2O phase increases after a 3 hour holding time treatment. In other words, as the holding time increases, there is an increasing proportion of generated Si_2N_2O phase. By extending the sintering holding time to 5 h, it is evident from the results that the physical phase structure primarily consists of O′-Sialon phase with a minor presence of SiC phase. Furthermore, as the

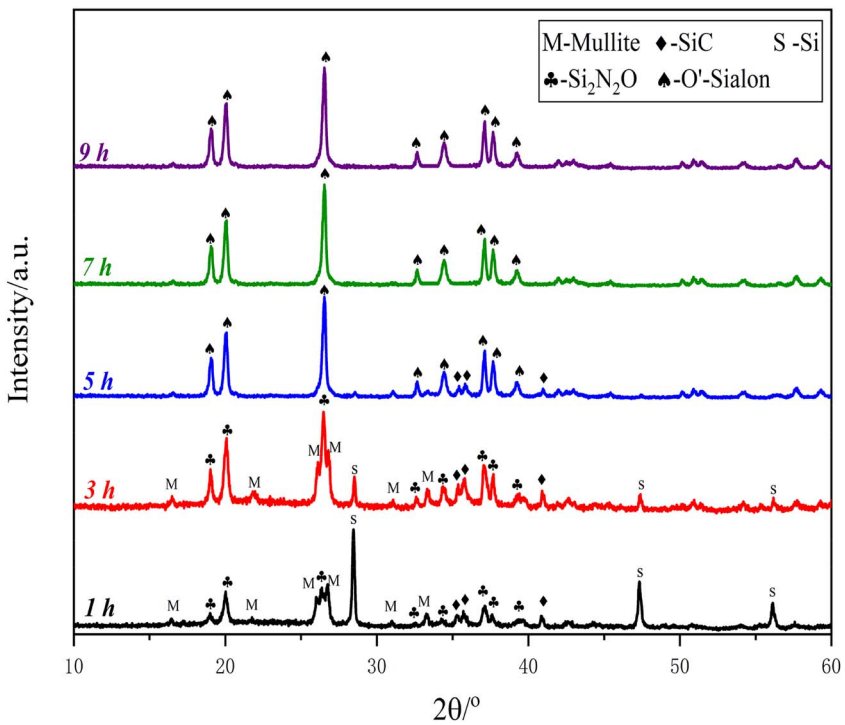

Fig. 6 XRD patterns of samples sintered at different holding times.

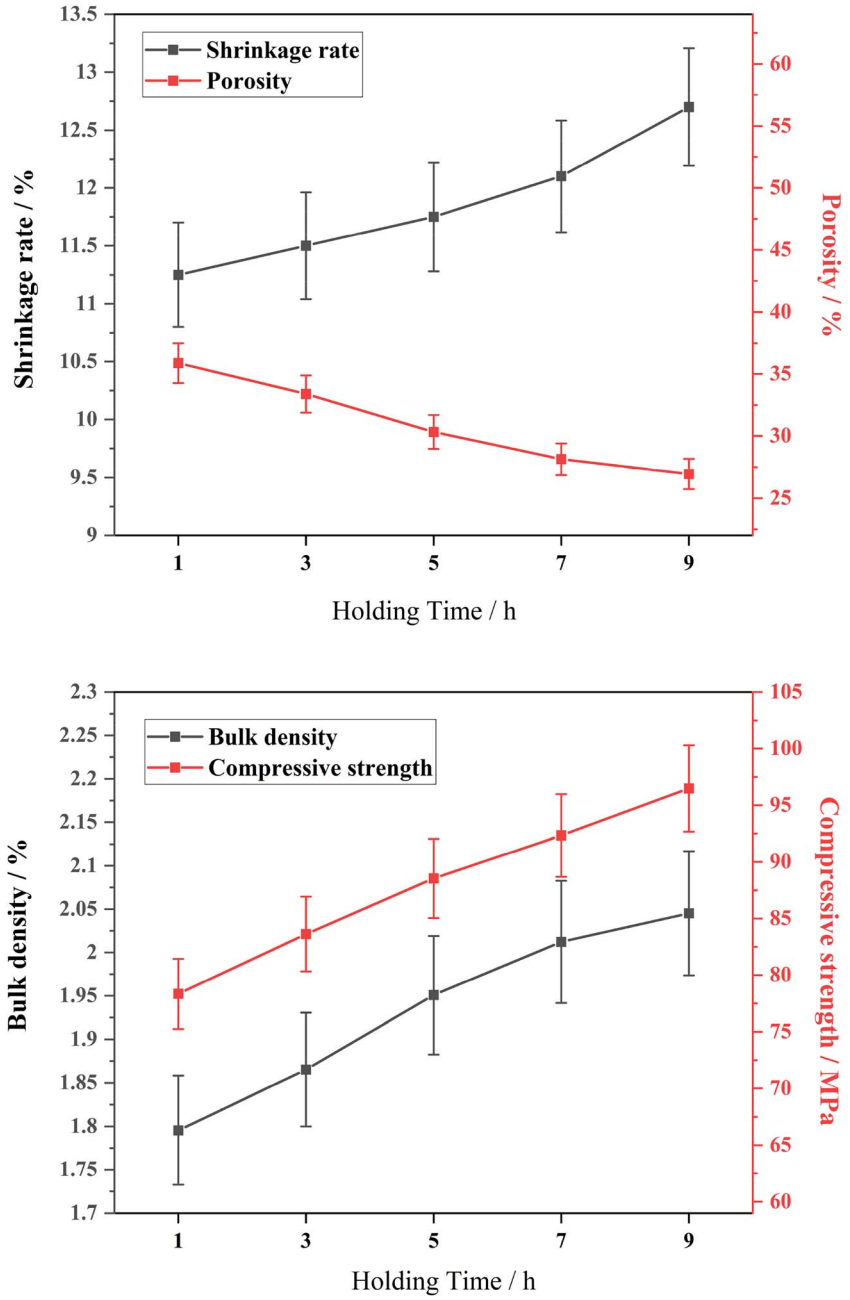

Fig. 7 Shrinkage, porosity, bulk density, and compressive strength of samples sintered at different holding times.

sintering holding time is extended to 7 h and 9 h, the physical phase composition remains dominated by O′-Sialon phase. Collectively, these findings indicate that at a holding time of 3 h, the synthesis reaction for the target product O′-Sialon does not occur; instead, intermediate products such as SiC and Si_2N_2O phases are formed prior to synthesis. However, after a sintering time of 5 h, successful generation of the desired product O′-Sialon is observed. With further extension of holding time, the O′-Sialon-dominant phase assemblage became more fully developed.

The performance parameters of the materials were analyzed under different sintering holding times, and the results are presented in Fig. 7. It can be observed that the overall performance of the materials gradually improves with increasing sintering treatment time. Specifically, as the sintering holding time is extended, there is an increase in sintering shrinkage from 11.25% to 12.7%, a decrease in porosity from 35.88% to 26.95%, an increase in compressive strength from 78.34 MPa to 96.48 MPa, and an increase in bulk density from 1.79 g cm^{-3} to 2.04 g cm^{-3}. Furthermore, by analyzing the physical phase composition using XRD, it can be inferred that with longer holding times, solid phase components undergo reactions leading to the formation of new crystalline phases which positively impact material performance.[31]

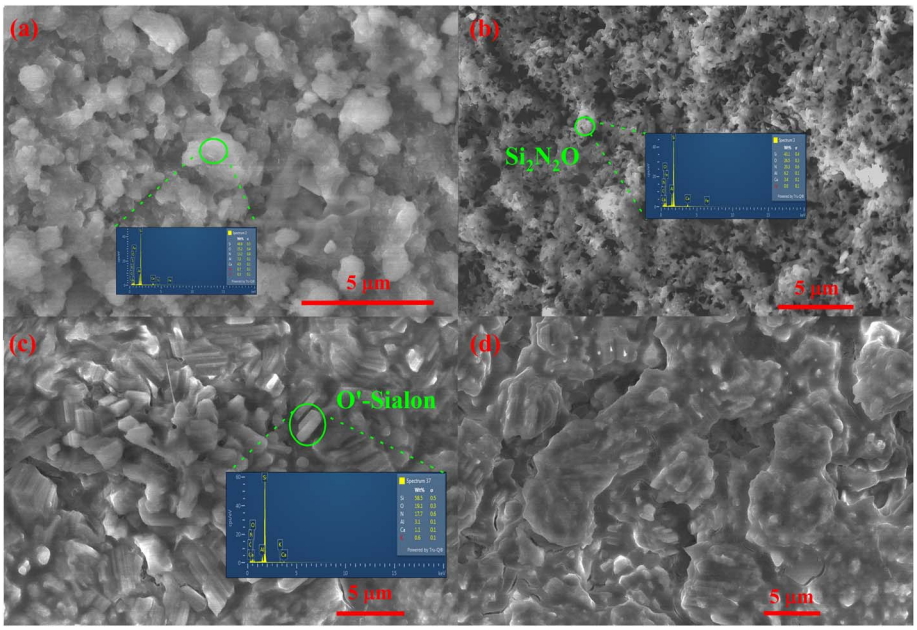

Fig. 8 SEM micrographs of HF-etched fragment surfaces of samples sintered at 1350 °C for various holding times: (a) 1 h, (b) 3 h, (c) 7 h, and (d) 9 h.

Table 2 The chemical composition of raw materials (wt%)

	Si	SiC	Al_2O_3					
SCW	38.126	59.963	1.723					
	SiO_2	Al_2O_3	CaO	Fe_2O_3	SO_3	TiO_2	MgO	K_2O
HAFA	47.998	38.373	4.607	3.399	2.891	1.285	0.561	0.53

The microstructural evolution of the HF-etched fragment surfaces at different holding times is shown in Fig. 8. The morphology changes significantly with increasing holding time. At a holding time of 1 h, the material still contains irregularly shaped particles, mainly composed of monocrystalline silicon and mullite phases. As the holding time increases to 3 h, a microstructure consisting of fine lamellar crystals is formed, which is identified as Si_2N_2O by compositional analysis. The relatively unusual morphology observed in Fig. 8(b) is attributed to a more porous local region dominated by intermediate Si_2N_2O-related microstructural features at 3 h, prior to the full development of the O′-Sialon-dominant product. Precipitation of long columnar crystals becomes evident at holding times of 7 h and 9 h. With prolonged sintering time, there is an increase in liquid phase generation at high temperatures, which subsequently cools down in a glassy phase encapsulated within grain boundaries. The results also demonstrate that an increase in holding time leads to microstructural changes, resulting in grain growth and an augmentation of the liquid phase. These alterations positively influence the macroscopic properties of the material.[32]

3.5 Migration and transformation of impurity elements

During the utilization of solid waste raw materials for O′-Sialon synthesis, it is crucial to consider both the presence of impurity elements and their transformation behavior during high temperature treatment. In this study, the primary composition of the raw material includes SCW and HAFA. Based on the raw-material composition data shown in Table 2, only minor impurity elements are present in SCW, whereas most impurity elements originate from HAFA. The composition of the raw materials after mixing is presented in Table 3, revealing that the primary impurity elements are CaO and Fe_2O_3, accompanied by a minor presence of SO_3. Furthermore, analysis of the TG results indicates that calcium in the fly ash exists as calcium sulfate, which decomposes at elevated temperatures (1000 °C) to generate CaO and release gaseous SO_2. Consequently, this study focuses solely on two elemental considerations: Ca and Fe. Prior to the analysis, the atmospheric composition during the heat treatment process was initially defined. High-purity nitrogen (99.5% purity) was introduced into the heat treatment procedure. It can be inferred that, under the experimental conditions, $P_{N_2} = 0.995P^{\theta}$, $P_{co} \approx 10 \times 10^{-3}P^{\theta}$ and $P_{O_2} \approx 4.5 \times 10^{-20}P^{\theta}$ (Fig. 9).

Table 3 The chemical composition of raw materials (wt%)

	Si	SiC	SiO_2	Al_2O_3	CaO	Fe_2O_3	SO_3	TiO_2	MgO	K_2O
Mixture	19.063	29.982	23.999	20.048	2.304	1.699	1.446	0.642	0.281	0.265

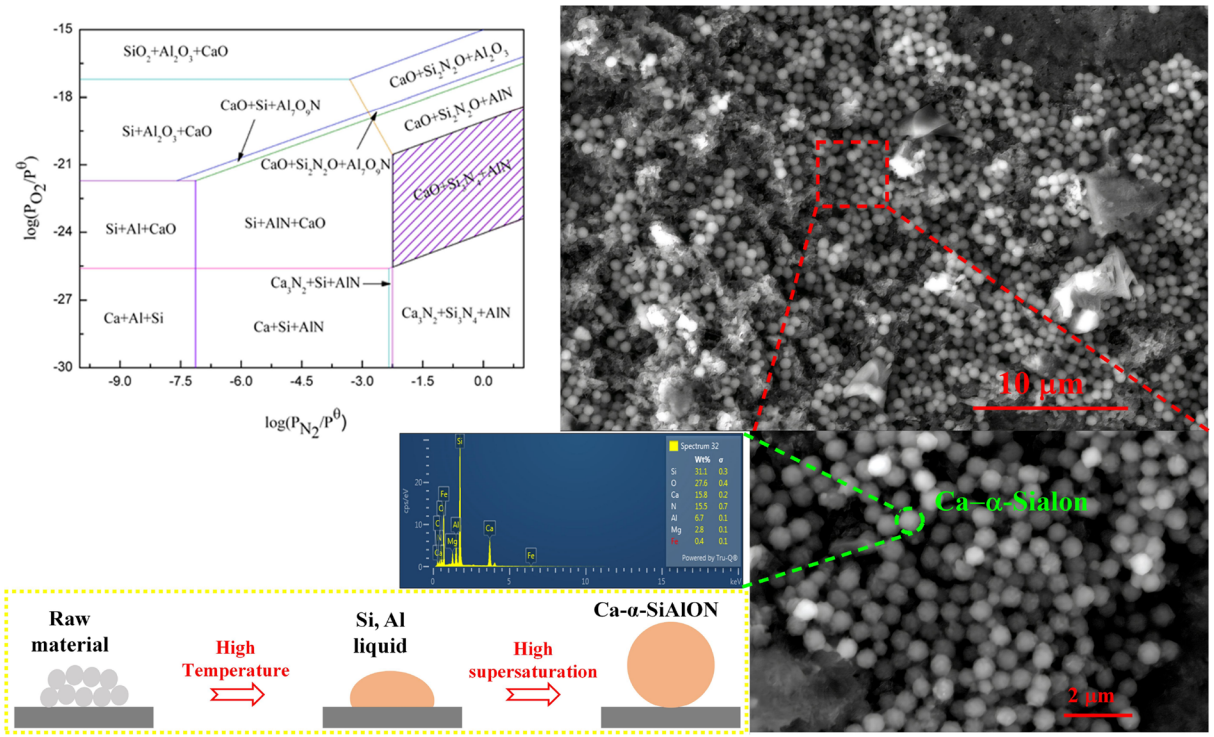

Fig. 9 Thermodynamic parameter state diagrams of Si–O–N and Ca–O–N systems at 1773 K and the microstructural result of sample sintered at 1350 °C for 5 h.

Firstly, in the phase diagram analysis, focusing on the direction of Ca element, it can be observed that under the atmospheric conditions of this study and at a temperature of 1823 K, Ca elements predominantly exist in the form of Ca-α-Sialon based on thermodynamic parameter state diagrams for stacked Si–O–N, Al–O–N, and Ca–O–N systems. Furthermore, through analysis of actual sintering results, spherical particles were found on the micro-morphology of samples processed by sintering and holding at 1350 °C for 5 h. EDS analysis revealed a high proportion of Ca element within these particles. To explain this phenomenon further: during high temperature processes involving impurity element Ca presence, liquid melt formation with raw materials containing Si and Al components occurs due to grain growth. According to model theory regarding grain morphology during liquid-phase sintering from a kinetic perspective; when diffusion rate exceeds solid/liquid interface reaction rate and there is a degree of supersaturation in surrounding liquid phase around grains as driving force for grain growth; low degrees result in noticeable differences in growth ability leading to anisotropic long columnar particle formation while high degrees result in less obvious differences resulting in larger equiaxed round particle development.[33] Therefore, under conditions where raw material components are enriched with Ca element as studied here; saturation levels within surrounding liquid phase affect Ca-α-SiAlON grain growth resulting in fine spherical particle formation.[34]

In order to address the changes in Fe element throughout the entire heat treatment process, an initial analysis was conducted to identify its source, which was found to primarily exist in the raw material HAFA. The Fe content in fly ash predominantly exists in the form of Fe_3O_4. Considering the specific composition characteristics of the raw materials used in this experiment, including monocrystalline silicon grinding and polishing waste as well as carbon overload, it is hypothesized that the following chemical reactions, shown in Table 4, may occur within the system.

Based on the data presented in the table and the standard Gibbs free energy changes shown in the graph (Fig. 10(a)), it is evident that all four reactions are heat-absorbing. The fourth reaction of Fe_3O_4 reduction to FeO exhibits the lowest Gibbs

Table 4 The Δ G^{θ} value of the reaction equation

	Reactions	Standard Gibbs free energy
1	$Fe_3O_4(s) + C(s) = 3FeO(s) + CO(g)$	$\Delta G^{\theta} = 182\,892.4–211.1T$ (J mol^{-1})
2	$Fe_3O_4(s) + 4C(s) = 3Fe(s) + 4CO(g)$	$\Delta G^{\theta} = 653\,460.3–658.5T$ (J mol^{-1})
3	$Fe_3O_4(s) + SiO_2(s) + 6C(s) = Fe_3Si(s) + 6CO(g)$	$\Delta G^{\theta} = 1\,222\,677–993.9T$ (J mol^{-1})
4	$Fe_3O_4(s) + CO(g) = 3FeO(s) + CO_2(g)$	$\Delta G^{\theta} = 30\,170–28.38T$ (J mol^{-1})

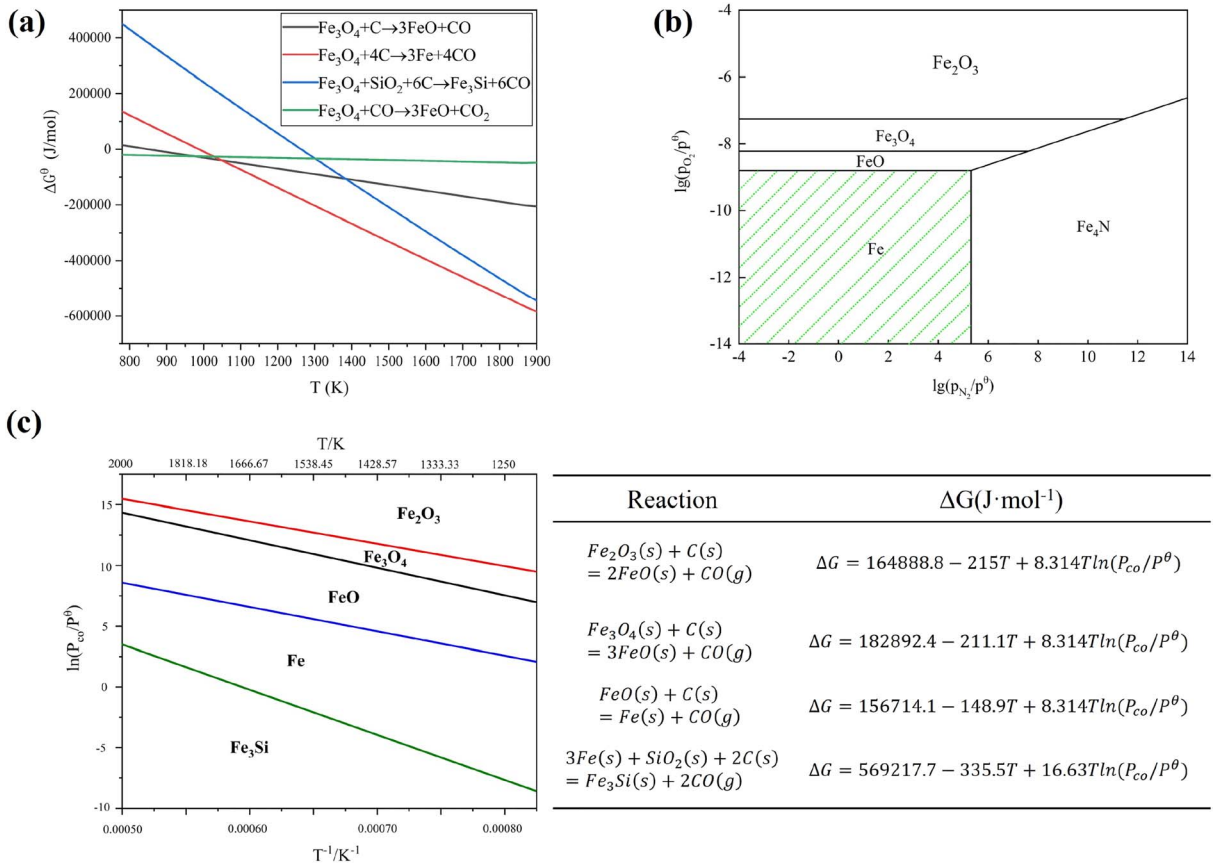

Reaction	$\Delta G(J\cdot mol^{-1})$
$Fe_2O_3(s)+C(s)=2FeO(s)+CO(g)$	$\Delta G = 164888.8-215T+8.314Tln(P_{co}/P^\theta)$
$Fe_3O_4(s)+C(s)=3FeO(s)+CO(g)$	$\Delta G = 182892.4-211.1T+8.314Tln(P_{co}/P^\theta)$
$FeO(s)+C(s)=Fe(s)+CO(g)$	$\Delta G = 156714.1-148.9T+8.314Tln(P_{co}/P^\theta)$
$3Fe(s)+SiO_2(s)+2C(s)=Fe_3Si(s)+2CO(g)$	$\Delta G = 569217.7-335.5T+16.63Tln(P_{co}/P^\theta)$

Fig. 10 (a) ΔG^θ_T-T relationship diagram of the reaction equation, (b) thermodynamic state diagram of Fe–O–N, (c) region diagram of stable existence of each substance in Fe–Si system with excess of C and SiO_2.

free energy below 1100 K. The Gibbs free energies of reactions 2 and 3 decrease rapidly with increasing sintering temperature, indicating a greater trend for reduction of Fe_3O_4 to Fe as well as for generation of Fe_3Si from Fe_3O_4 *vs.* SiO_2. The reaction with the lowest Gibbs free energy for generating Fe suggests that this trend is most pronounced at high temperatures and results in a stable phase of generated Fe. Considering atmospheric partial pressure effects on product formation, thermodynamic parameters were plotted for the Fe–O–N system at 1873 K based on literature data. Under experimental conditions used in this project, nitrogen has a partial pressure of 0.995 P^θ while oxygen has a partial pressure of $4.5\times10^{-20}\ P^\theta$; thus, metallic Fe is predicted to be the stable Fe-bearing phase according to Fig. 10(b).

The thermodynamic parameter state diagram presented above is constructed based on the consideration of Fe, O, and N only. However, in the actual reaction process, there are abundant amounts of C and SiO_2 present. Under these conditions, Fe will continue to react with sufficient C and SiO_2 to form new substances. Therefore, it is necessary to reanalyze the behavior of Fe under these specific conditions. Since the reaction takes place in a flowing nitrogen atmosphere containing ample amounts of C and SiO_2, the formation of CO gas should occur as a reaction product. The partial pressure (P_{co}) of CO gas will inevitably exert a significant influence on the overall reaction results. Therefore, based on the correlation between the Gibbs free energy of specific reactions and temperature as well as CO partial pressure, we have constructed a phase diagram illustrating the dominant region in the Fe–Si system under an excess of C and SiO_2. It should be noted that $P_{co}=10\times10^{-3}P^\theta$ *i.e.*, $\ln P_{co}/P^\theta=-4.6$ under our experimental conditions. As depicted in Fig. 10(c), Fe exists predominantly in the form of Fe_3Si within our experimental atmosphere. Furthermore, it is worth mentioning that increasing temperature, enhancing N_2 flow rate, and reducing CO partial pressure all contribute favorably to the formation of Fe_3Si.

4. Conclusion

O′-Sialon-based ceramics were successfully synthesized from SCW and HAFA through a carbothermal reduction–nitridation route. Thermal analysis provided an indicative temperature window for phase evolution, and the sintering experiments confirmed that 1350 °C is the critical temperature for obtaining an O′-Sialon-dominant phase assemblage in the present system, whereas higher temperatures promote the formation of β-Sialon. At 1350 °C, a holding time of about 5 h was required for full development of the O′-Sialon-dominant product. Increasing temperature or holding time improved densification and compressive strength through progressive reaction, grain development, and liquid-phase-assisted sintering. Thermodynamic analysis together with microstructural observations

further suggests that Ca is redistributed into Ca-containing SiAlON-related phases, while Fe is mainly stabilized as Fe3Si. These results demonstrate the feasibility of converting SCW and HAFA into value-added SiAlON-based ceramics, although further work is still needed to assess raw-material variability, process reproducibility, and scale-up.

Author contributions

Hao Wang: conceptualization, data curation,formal analysis, investigation, methodology, visualization,writing – original draft. Xinlin Zhai: data curation, formal analysis, methodology, validation, visualization. Lili Liu: formal analysis,investigation,methodology, validation. Yin Jiang: formal analysis,investigation,methodology. Yi Xing: funding acquisition,project administration, resources, supervision, writing – review & editing.

Conflicts of interest

The authors declare no competing interests.

Data availability

The data supporting the findings of this study are not publicly available in order to protect the privacy of the research participants. However, they can be obtained from the corresponding author Hao Wang, email: wanghao@ustb.edu.cn] upon reasonable request and subject to ethical approvals and data protection regulations.

Acknowledgements

This research was funded by the National Natural Science Foundation of China (52304418).

References

1 J. W. Guo, X. M. Liu, J. M. Yu, *et al.*, An overview of the comprehensive utilization of silicon-based solid waste related to PV industry, *Resour. Conserv. Recycl.*, 2021, **169**, 105450.
2 Q. Zhang, C. J. Yu, J. Fang, *et al.*, Using the combined fenton-MBR process to treat cutting fluid wastewater, *Pol. J. Environ. Stud.*, 2017, **26**, 1375–1383.
3 K. X. Wei, S. C. Yang, X. H. Wan, *et al.*, Review of silicon recovery and purification from saw silicon powder, *JOM*, 2020, **72**, 2633–2647.
4 H. S. G. K. Murthy, Evolution and present status of silicon carbide slurry recovery in silicon wire sawing, *Resour. Conserv. Recycl.*, 2015, **104**, 194–205.
5 D. Wei, S. Gao, J. Kong, *et al.*, Recycling silicon from silicon cutting waste by Al-Si alloying, *J. Clean. Prod.*, 2020, **251**, 119647.
6 Z. Wang, D. Wang, Z. Wang, *et al.*, Centrifugal field enhanced oilwater phase separate in Si/SiC separation process of silicon wire-saw waste, *Chin. J. Process Eng.*, 2019, **19**, 119–125.
7 X. Li, J. Wu, M. Xu and W. Ma, Separation and purification of silicon from cutting kerf-loss slurry waste by electromagnetic and slag treatment technology, *J. Clean. Prod.*, 2019, **211**, 695–703.
8 M. Xu, L. Gao, H. Chen and L. Guo, Study on SiC porous ceramics with the preparation of retrieve cut metal silicon-spindle wire, *Ceram. Int.*, 2009, **45**, 24–26.
9 X. Jin, J. Kong, J. Wang, *et al.*, Preparation of high-purity silicon nitride from diamond-wire cutting waste, *Chin. J. Appl. Chem.*, 2018, **35**, 1364–1370.
10 Y. Sun, H. Tang, L. Li and Y. Sun, Preparation of Si_3N_4 bonded SiC refractories from waste slurry of cutting silicon, *Refractories*, 2012, **46**, 450–455.
11 B. H. Chen, S. I. Chuang, W. Liu and J. G. Duh, A Revival of Waste: atmospheric Pressure Nitrogen Plasma Jet Enhanced Jumbo Silicon/Silicon Carbide Composite in Lithium-Ion Batteries, *ACS Appl. Mater. Interfaces*, 2015, **7**, 28166–28176.
12 Y. Hou, G. H. Zhang and K. C. Chou, Preparation of α-Si3N4 by direct nitridation using polysilicon waste by diamond wire cutting, *Int. J. Appl. Ceram. Technol.*, 2020, **17**, 84–93.
13 X. Jin, J. Kong, X. T. Zhou, *et al.*, Recycling of silicon kerf loss derived from diamond-wire saw cutting process to prepare silicon nitride, *J. Clean. Prod.*, 2020, **247**, 119163.
14 Q. Y. Sun, L. Yuan, E. D. Jin, *et al.*, Transformation of polysilicon cutting waste into SiC/α-Si3N4 composite powders via electromagnetic induction heating, *Ceram. Int.*, 2021, **47**(9), 12269–12275.
15 H. Wang, Z. W. Chen, Z. Meng, *et al.*, Integrated utilization of coal gangue for synthesis of β-Sialon multiphase ceramic materials, *Ceram. Int.*, 2023, **49**, 11275–11284.
16 H. C. Liu, B. L. Wang, Y. X. He, *et al.*, Significantly enhanced thermal shock resistance of α-Si_3N_4/O'-Sialon composite coating toughened by two-dimensional h-BN nanosheets on porous Si_3N_4 ceramics, *Ceram. Int.*, 2022, **48**(20), 30510–30516.
17 H. Q. Ma and C. G. Bao, Preparation, oxidation property and mechanism of Si_3N_4/O'-SiAlON composite ceramics, *Ceram. Int.*, 2021, **47**, 15383–15391.
18 J. C. An, T. Z. Ge, E. X. Xu, *et al.*, Preparation and properties of mullite-SiC-O'-SiAlON composites for application in cement kiln, *Ceram. Int.*, 2020, **46**, 15456–15463.
19 K. Z. Dou, Y. S. Jiang, B. Xue, *et al.*, The carbon environment effects on phase composition and photoluminescence properties of β-SiAlON multiphase materials prepared from fly ash acid slag, *Ceram. Int.*, 2019, **45**, 7850.
20 D. A. Gunn, A theoretical evaluation of the stability of sialon-bonded silicon carbide in the blast furnace environment, *J. Eur. Ceram. Soc.*, 1993, **11**(1), 35–41.
21 P. Jiang, X. F. Wu, W. D. Xue, *et al.*, In-situ synthesis and reaction mechanism of β-SiAlON in the Al-Si_3N_4-Al_2O_3 composite material, *Ceram. Int.*, 2017, **43**, 1335.
22 H. Wang, Z. W. Chen, R. Ji, *et al.*, Integrated utilization of high alumina fly ash for synthesis of foam glass ceramic, *Ceram. Int.*, 2018, **44**, 13681–13688.

23 H. Wang, Y. Q. Sun, L. L. Liu, *et al.*, Integrated utilization of fly ash and waste glass for synthesis of foam/dense bi-layered insulation ceramic tile, *Energy Build.*, 2018, **168**, 67–75.
24 Y. Shao, X. L. Li, H. M. Ji, *et al.*, Effect of α-Al_2O_3 on in situ synthesis low density O' -sialon multiphase ceramics, *J. Alloys Compd.*, 2011, **509**, 8345–8349.
25 F. Z. Guo, Z. B. Yin and J. T. Yuan, Phase transformation kinetics and grain orientation of multi-cation doped (Yb, Sm) α/β-SiAlON ceramic tool materials, *Ceram. Int.*, 2023, **49**, 27983–27992.
26 L. Y. Li, G. L. Gao, G. L. Chang, *et al.*, Effect of β-SiAlON content on the sintering and bacteriostatic properties of β-SiAlON-Si_3N_4 composite ceramics, *Ceram. Int.*, 2022, **48**, 33704–33711.
27 L. G. Zhang, C. Zhang, E. X. Xu, *et al.*, Effect of ZrO_2 on the physicochemical properties and biological properties of β-SiAlON-ZrO_2 composite ceramics, *Ceram. Int.*, 2021, **47**(1), 1244–1252.
28 X. Q. Yan, A brief evaluation of approximation methods for microcrack shielding problems, *Trans. ASME, J. Appl. Mech.*, 2006, **73**(4), 694–696.
29 J. F. Wu, C. J. Ding, X. H. Xu and K. F. Mi, Effects of Gd_2O_3 and Yb_2O_3 on the microstructure and performances of O'-Sialon/Si_3N_4 ceramics for concentrated solar power, *Ceram. Int.*, 2021, **47**, 5054–5060.
30 C. Y. Xi, H. S. Guo, C. X. Zhang and J. T. Luo, Preparation of O'-Sialon-based ceramics by two-stage liquid phase sintering and study on the toughening mechanism of ultrafine-grained sintered clusters, *Ceram. Int.*, 2022, **48**, 9362–9370.
31 X. X. Xue, T. Jiang, J. Yang and P. Xie, Properties and application of O'-Sialon matrix ceramics, *J. Mater. Metall.*, 2002, **1**, 25–30.
32 H. Wang, M. G. Zhu, Y. Q. Sun, *et al.*, Synthesis of a ceramic tile base based on high-alumina fly as, *Constr. Build. Mater.*, 2017, **155**, 930–938.
33 M. Krämer, M. J. Hoffmann and G. Petzow, Grain Growth Studies of Silicon Nitride Dispersed in an Oxynitride Glass, *J. Am. Ceram. Soc.*, 1993, **76**(11), 2753.
34 H. Yurdakul and S. Turan, Incorporation of the transition metals (Cr and Fe) into β-SiAlON crystal structure, *Ceram. Int.*, 2011, **37**(5), 1501–1505.